Journal of Hazardous Materials 183 (2010) 51–61

Contents lists available at ScienceDirect

Journal of Hazardous Materials

journal homepage: www.elsevier.com/locate/jhazmat

Numerical simulations of LNG vapor dispersion in Brayton Fire Training Field tests with ANSYS CFX

Ruifeng Qi, Dedy Ng, Benjamin R. Cormier, M. Sam Mannan*

Mary Kay O'Connor Process Safety Center, Artie McFerrin Department of Chemical Engineering, Texas A&M University System, College Station, TX 77843-3122, USA

ARTICLE INFO

Article history:
Received 9 August 2009
Received in revised form 20 June 2010
Accepted 21 June 2010
Available online 1 July 2010

Keywords:
LNG
Vapor dispersion simulation
ANSYS CFX
Field test

ABSTRACT

Federal safety regulations require the use of validated consequence models to determine the vapor cloud dispersion exclusion zones for accidental liquefied natural gas (LNG) releases. One tool that is being developed in industry for exclusion zone determination and LNG vapor dispersion modeling is computational fluid dynamics (CFD). This paper uses the ANSYS CFX CFD code to model LNG vapor dispersion in the atmosphere. Discussed are important parameters that are essential inputs to the ANSYS CFX simulations, including the atmospheric conditions, LNG evaporation rate and pool area, turbulence in the source term, ground surface temperature and roughness height, and effects of obstacles. A sensitivity analysis was conducted to illustrate uncertainties in the simulation results arising from the mesh size and source term turbulence intensity. In addition, a set of medium-scale LNG spill tests were performed at the Brayton Fire Training Field to collect data for validating the ANSYS CFX prediction results. A comparison of test data with simulation results demonstrated that CFX was able to describe the dense gas behavior of LNG vapor cloud, and its prediction results of downwind gas concentrations close to ground level were in approximate agreement with the test data.

1. Introduction

Natural gas has become one of the fastest growing sources of energy in the United States. This growth has been driven by the needs for cleaner energy, the relative low price of natural gas, and its abundant supplies. By implementing advanced liquefaction technology, natural gas can be purified and refrigerated into a liquid (LNG), which makes it easier to transport and store in tankers. Many onshore or offshore LNG import terminals have been proposed and are expected to be constructed in the next several years to meet the projected significant increase in LNG importation from overseas as a result of growing demand [1,2].

As LNG import terminal and facility construction increases, concerns about the potential hazards that LNG spills could pose have been raised. One of the major hazards from an accidental LNG release is the formation of a flammable vapor cloud, which drifts downwind near the ground for a certain time until it completely warms up and dissipates in the atmosphere. If an ignition source is present and vapors mix with air in its flammability range, the vapor cloud will ignite and burn [3]. To ensure public safety in adjacent populated areas, federal regulation 49 CFR Part 193 [4] and standard NFPA 59A [5] have required LNG industries to use validated consequence models to predict potential hazardous areas (exclusion zones) around LNG facilities in the event of an accidental LNG release.

Consequence modeling of accidental LNG releases has been studied extensively as part of the effort extended to prevent and mitigate such incidents. Two types of major LNG vapor dispersion models are integral models and computational fluid dynamics (CFD) models. Integral models such as DEGADIS, SLAB, HEGADAS, and many others are widely used because of their fast computational time and ease of use [6–8]. However, most integral models have limitations in describing the terrain and congestion density of obstacles in LNG spill scenarios, whose effects on vapor cloud and turbulence cannot be neglected in modeling vapor dispersion [9]. Recent advancements in computation capabilities, including processing capacity and memory space, have made it possible for engineers to use CFD to solve complex fluid flow problems. CFD models are able to provide a detailed description of physical processes and handle complex geometries, and can thus be used to predict the behavior of LNG vapor cloud dispersion in a site-specific risk analysis [10–15]. However, CFD simulation setup methods for LNG vapor dispersion and their validation against actual large or medium-scale spill tests have not been sufficiently reported in the literature.

Since 2005, BP Global Gas SPU and the Mary Kay O'Connor Process Safety Center (MKOPSC) have jointly established a research and development program to investigate LNG spill emergency

* Corresponding author. Tel.: +1 979 862 3985; fax: +1 979 458 1493.
E-mail address: mannan@tamu.edu (M.S. Mannan).

0304-3894/$ – see front matter © 2010 Elsevier B.V. All rights reserved.
doi:10.1016/j.jhazmat.2010.06.090

Nomenclature

A_p	pool area (m^2)
C_μ	turbulence constant (0.09)
CFD	computational fluid dynamics
D	pool diameter (m)
k	turbulence kinetic energy (m^2/s^{-2})
L	Monin–Obukhov length (m)
LFL	lower flammable limit
LNG	liquefied natural gas
$\dot{m}_{liq}$	LNG mass flow rate (kg/s)
P	pressure (Pa)
P_0	standard reference pressure (Pa)
$\dot{Q}$	heat flux (W/m^2)
T	temperature (K)
T_i	turbulence intensity
U	velocity (m/s)
U_*	friction velocity (m/s)
U_x	x-component velocity (m/s)
U_y	y-component velocity (m/s)
U_z	z-component velocity (m/s)
UFL	upper flammable limit
$\dot{V}$	volume flow rate (m^3/s)
v_g	vapor velocity (m/s)
$\dot{y}$	liquid regression rate (m/s)
z	vertical height (m)
z_0	surface roughness height (m)

Greek letters

α	angle (rad)
ε	turbulence eddy dissipation rate (m^2/s^3)
θ	potential temperature (K)
θ_*	scaling potential temperature (K)
θ_0	potential temperature at z_0 (K)
κ	von Karman constant (0.41)
λ	liquid latent heat of vaporization (J/kg)
ρ_g	LNG vapor density at the boiling point (kg/m^3)
ρ_L	liquid density (kg/m^3)

response and hazard control. A series of medium-scale field tests have been performed at the Brayton Fire Training Field (BFTF), which is affiliated with the Texas A&M University system. As part of this program, experimental data collected from these tests are utilized to study the physical behavior of vapor dispersion in the atmosphere and to validate consequence model prediction results. In the present work, ANSYS CFX 11.0 was used to perform simulations of LNG vapor dispersion whose results would then be validated with LNG spill experiments at BFTF. Here, we report the important parameters for setting up the LNG vapor dispersion simulation using ANSYS CFX. Essential inputs associated with the domain and boundary conditions are discussed. The quality of simulation results is always influenced by uncertainties or errors of parameters related to the numerical methods and physical models. Thus, a sensitivity analysis was conducted to illustrate the impact of the mesh size and source term turbulence intensity on predicting safe separation distances (distance to the half lower flammable limit, 1/2 LFL). The motivation of this work was to provide guidance in modeling LNG vapor dispersion with ANSYS CFX, which can be used to evaluate the design, siting, and layout of LNG plants.

2. Simulation setup with ANSYS CFX

The ANSYS CFX is a general-purpose CFD package capable of solving diverse and complex three-dimensional fluid flow problems. ANSYS CFX uses the Navier–Stokes equations to describe the fundamental processes of momentum, heat, and mass transfer. It also incorporates a number of mathematical models that can be used together with the Navier–Stokes equations to describe other physical or chemical processes such as turbulence, combustion, or radiation. Like most commercial CFD packages, ANSYS CFX uses a finite volume approach to convert the governing partial differential equations into a system of discrete algebraic equations by discretizing the computational domain. These equations may result in a solution with specified domain boundary conditions. For a transient simulation, an initial condition is also required to numerically close the equations. One of the most important features of CFX is that it uses a coupled solver, which solves the fluid flow and pressure as a single system and faster than the segregated solver up to a certain number of control volumes as it requires fewer iterations to achieve equally converged solutions [16,17].

Table 1
Summary of input variables for LNG vapor dispersion simulation setup.

Components	Inputs (parameters)
Geometry creation	3D geometry (terrain and obstacles)
Meshing	Mesh shape and size
Pre-processing—domain	Fluid properties Turbulence model Heat transfer model Buoyancy model
Pre-processing—atmosphere boundary	Fluid composition Wind direction and velocity profile Temperature profile Turbulence profile
Pre-processing—LNG pool boundary	Fluid composition Vapor evaporation velocity Vapor temperature Turbulence
Pre-processing—ground boundary	Influence on flow Surface roughness height Surface temperature or heat flux

The basic procedure in modeling LNG vapor dispersion with ANSYS CFX consists of five steps—creating the geometry, meshing, pre-processing, solving, and post-processing. With regard to simulation setup, only the first three steps are considered. Table 1 lists all the essential inputs or parameters in the setup process. Details of the inputs in Table 1 are described in the following sections.

2.1. Creating the geometry

The first step in a CFD simulation is to create the geometry of the flow field. The flow field of interest is represented by a computational domain within which the equations of fluid flow and heat transfer are solved. Considering one of the primary advantages of CFD models is that it is capable of handling complex geometries, the appropriate geometry must be built or imported to represent the features of flow field that impact the simulated variables of interest. When modeling LNG vapor dispersion, obstacles and terrain near the source or in the traveling path of the LNG vapor downwind must be constructed in the domain to account for their effects on the vapor cloud; otherwise, the CFD analysis may overestimate or underestimate the hazardous area. Some geometries can contribute to an increase in vapor concentrations by lowering the wind speed or decreasing the atmospheric turbulence, while others can reduce the downwind vapor concentrations by trapping the vapor within the source area or diluting in the turbulent wake of obstacles [18].

2.2. Meshing

The second step is subdividing the computational domain. The domain is discretized into a number of small control volumes using a mesh generated by CFX-Mesh. The mesh had structured grids in the near-wall regions and unstructured grids in the bulk of domain, which contains tetrahedral, pyramid and prismatic elements. ANSYS CFX provides a list of criteria to assess the quality of the mesh through mesh-associated parameters such as the edge length ratio, maximum and minimum face angle, connectivity number, and element volume ratio [19]. The mesh size must be chosen carefully to avoid the adverse effect on the simulation accuracy. A recommended approach to eliminate mesh size influence is to seek mesh-independent solutions by testing with gradually reduced mesh sizes until the simulation results no longer change [20–22].

2.3. Domain and boundary conditions

2.3.1. Domain

ANSYS CFX is not designed especially as a consequence model for LNG spill hazards, and therefore fluid properties and physical models must be identified to characterize the physical process of LNG vapor dispersion when defining the domain. Detailed explanations and the selection of these properties are described as follows.

LNG is mainly composed of methane, but may also contain small amounts of ethane, propane, and heavier hydrocarbons [23]. When LNG is released from containment onto land or water, it forms a pool that generates a visible LNG vapor cloud. As LNG evaporates, the methane vaporizes faster than the heavier components due to its lower boiling point. As a result, vapor will be preferentially methane rich, whereas the heavier components will stay in the liquid pool [24]. Therefore, the thermodynamic properties of methane can be used as a proxy to LNG vapor properties. When performing a dispersion simulation, the properties of a mixture corresponding to the composition of LNG must be specified as the fluid properties.

The dispersion of a vapor cloud in the atmosphere goes through three stages: negative buoyancy, neutral buoyancy, and positive buoyancy, depending on the temperature of the vapor cloud. At a temperature of 166 K, the density of methane is almost identical to that of air at a temperature of 289 K. Below 166 K, methane is negatively buoyant and more likely to accumulate in low areas. When the temperature is above 166 K, LNG vapor is positively buoyant and dissipates more easily in open areas, posing little flammable hazard to people and property on the ground [24]. If the release occurs in confinement, the buoyant vapor cloud is still hazardous as it might lead to a vapor cloud explosion. As the temperature increases, the LNG dispersion status changes from negative to positive buoyancy. Therefore, a buoyancy model is required to capture the density difference caused by the temperature variation. In ANSYS CFX, the full buoyancy model is recommended for simulating the buoyancy effect given that the fluid density is a function of temperature. Within this model, the buoyancy reference density can be set to 1.225 kg/m^3 [15].

Similarly, a turbulence model must be identified to predict the effects of turbulence in the ambient atmosphere and LNG vapor. ANSYS CFX offers a large variety of turbulence models, such as the k–ε model, k–ω model, and shear stress transport (SST) model [16]. A comparative study of these turbulence models against experimental data has been reported elsewhere [25]. In the present work, the standard k–ε model was used because of its balance between computational time and precision. This model has been used for numerical simulations of LNG vapor dispersion and other dense gas dispersions with satisfactory results [12,13,26].

Finally, a heat transfer model is selected to represent the heat transfer throughout fluids within the domain. This model must take into account both the thermal energy and kinetic energy, which can be addressed in ANSYS CFX using the total energy model.

2.3.2. Atmosphere boundary

The atmospheric surface layer is the region of interest where LNG vapor dispersion occurs following an accidental release. An accurate description of air flow in the atmospheric surface layer near the ground is of prime importance to make CFD codes generate reliable simulation results. Almost all atmosphere-related simulations have modeled the air flow in this layer as fully developed horizontally homogeneous, in which the mean variables are only dependent on the height z. In a simulation with ANSYS CFX, the atmospheric boundary is always set as an open boundary, where fluids can simultaneously flow in and out of the domain. Wind velocity, temperature, and turbulence profiles are developed to represent the characteristics of these variables in real situations. In the atmospheric surface layer, the momentum and heat vertical fluxes do not vary by more than 10%. Due to these small flux variations, the use of the Monin–Obukhov similarity theory is recommended to describe the wind velocity, temperature, and turbulence profiles [10,27]. The wind velocity and potential temperature gradient functions along the height z are given as follows [28]:

$$\frac{\partial U}{\partial z} = \frac{U_*}{k \cdot z} \cdot \phi_m \left(\frac{z}{L}\right) \tag{1}$$

$$\frac{\partial \theta}{\partial z} = \frac{\theta_*}{k \cdot z} \cdot \phi_h \left(\frac{z}{L}\right) \tag{2}$$

where L, U_*, and θ_* are the Monin–Obukhov length, friction velocity, and scaling potential temperature, respectively, and κ is the von Karman constant (0.41).

Integrating the above equations from z_0 to z gives:

$$U(z) = \frac{U_*}{k}\left[\ln\left(\frac{z}{z_0}\right) - \psi_m\left(\frac{z}{L}\right)\right] \tag{3}$$

$$\theta(z) = \theta_0 + \frac{\theta_*}{k}\left[\ln\left(\frac{z}{z_0}\right) - \psi_h\left(\frac{z}{L}\right)\right] \tag{4}$$

where

$$\psi_m\left(\frac{z}{L}\right) = \int_{z_0}^{z}\left(\frac{1}{z} - \frac{\phi_m(z/L)}{z}\right)dz \tag{5}$$

$$\psi_h\left(\frac{z}{L}\right) = \int_{z_0}^{z}\left(\frac{1}{z} - \frac{\phi_h(z/L)}{z}\right)dz \tag{6}$$

here z_0 is the surface roughness height and θ_0 is the potential temperature at z_0.

The potential temperature is related to the ambient temperature and pressure by

$$\theta = T\left(\frac{P_0}{P}\right)^{\mu} \tag{7}$$

where T is the actual temperature, P is the actual pressure, P_0 is the standard reference pressure, and $\mu = 0.285$. Generally, the potential and actual temperatures in the atmospheric surface layer, in absolute units, do not differ by more than 10% [29].

The Cartesian components of the wind velocity in three directions are then expressed by introducing the wind direction angle α:

$$U_x(z) = U(z) * \cos(\alpha) \tag{8}$$

$$U_y(z) = U(z) * \sin(\alpha) \tag{9}$$

$$U_z(z) = 0 \tag{10}$$

Air flow in the atmospheric surface layer is a type of external flow, which means the air flows over or across objects rather than

through them. In such a case, ANSYS CFX cannot automatically calculate the turbulence characteristics, such as turbulence kinetic energy k and eddy dissipation rate ε. One approach to deal with this limitation is to relate these variables to the Monin–Obukhov length [30]:

$$k(z) = 5.48U_*^2\left[\frac{\phi_h(z/L)}{\phi_m(z/L)}\right]^{1/2} \tag{11}$$

$$\epsilon(z) = \frac{U_*^3}{k\cdot z}\phi_h\left(\frac{z}{L}\right) \tag{12}$$

The functions $\phi_m(z/L), \phi_h(z/L), \psi_m(z/L), \psi_h(z/L)$ can be expressed as empirical relations with the Monin–Obukhov length [28]:

When $L>0$

$$\phi_m\left(\frac{z}{L}\right) = \phi_h\left(\frac{z}{L}\right) = 1+5\frac{z}{L} \tag{13}$$

$$\psi_m\left(\frac{z}{L}\right) = \psi_h\left(\frac{z}{L}\right) = -5\frac{z}{L} \tag{14}$$

When $L<0$

$$\phi_m\left(\frac{z}{L}\right) = \frac{1}{x} \tag{15}$$

$$\phi_h\left(\frac{z}{L}\right) = \frac{1}{x^2} \tag{16}$$

$$\psi_m\left(\frac{z}{L}\right) = 2\ln\left[\frac{1+x}{2}\right] + \ln\left[\frac{1+x^2}{2}\right] - 2\tan^{-1}(x) + \frac{\pi}{2} \tag{17}$$

$$\psi_h\left(\frac{z}{L}\right) = 2\ln\left[\frac{1+x^2}{2}\right] \tag{18}$$

with

$$x = \left(1-\frac{16z}{L}\right)^{1/4} \tag{19}$$

To solve the above equations, the wind velocity and temperature must be measured at least at two different heights above the ground. Another alternative approach to represent the wind velocity and turbulence profiles associated with the k–ε turbulence model if measurements are made at only one height is proposed as follows [31]:

$$U = \frac{U_*}{k}\ln\left(\frac{z+z_0}{z_0}\right) \tag{20}$$

$$k = \frac{U_*^2}{\sqrt{C_\mu}} \tag{21}$$

$$\varepsilon = \frac{U_*^2}{k(z+z_0)} \tag{22}$$

With this method, the temperature is assumed to be constant along the height z.

2.3.3. LNG pool

The LNG pool can be specified as an inlet boundary, where the LNG vapor flows into the domain. The LNG pool area and shape, evaporation rate, vapor temperature, and turbulence in the source term are essential parameters required to describe the LNG pool boundary.

The pool area and shape depend on the surface properties and geometry of the spill area. When there is a release in an impoundment area, the LNG pool keeps the same area and shape as the impoundment due to the presence of boundaries. For an instantaneous release or continuous release of LNG in an open area, pool spreading models are required to determine the spread rate and area [32–34]. The commonly used model for calculating the free-spreading pool area in the case of continuous LNG release on water is [35]:

$$A_p = \frac{\dot{V}}{\dot{y}} \tag{23}$$

where $\dot{V}$ is the mean spill rate, A_p is the pool area, and $\dot{y}$ is the mean liquid regression rate,

$$\dot{y} = \frac{\dot{Q}}{\rho_L\lambda} \tag{24}$$

here $\dot{Q}$ is the mean heat flux to the pool, ρ_L is the liquid density, and λ is the liquid latent heat of vaporization.

The mean vapor velocity across the pool entering the domain can be determined by

$$v_g = \frac{\dot{m}_{liq}}{\rho_g\cdot A_p} \tag{25}$$

where v_g is the vapor velocity, $\dot{m}_{liq}$ is the LNG mass flow rate, and ρ_g is the LNG vapor density at the boiling point.

The recommended vapor temperature at this boundary is 111 K, which is the LNG boiling point under normal conditions.

The turbulence above the pool induced by vapor evaporation must be specified as part of the k–ε model requirements. The following equations provide the relationship between the turbulence kinetic energy and the energy dissipation rate with the turbulence intensity [10]:

$$k = \frac{3}{2}(v_g T_i)^2 \tag{26}$$

$$\varepsilon = C_\mu^{3/4}\frac{k^{3/2}}{0.07D} \tag{27}$$

where C_μ is the turbulence constant (0.09), T_i is the turbulence intensity and D is the LNG pool diameter.

2.3.4. Ground

The ground is set as a no-slip condition, which means the velocity on the surface is zero. Basic parameters that must be specified at the ground boundary include the heat flux or surface temperature. The heat flux from the ground to the atmosphere can be positive or negative, depending on the temperature difference between the ground and atmosphere. Terrain and obstacles can be represented as geometrical features of the ground. The roughness of their surfaces in ANSYS CFX is expressed in terms of a roughness height or equivalent sand grain roughness, whose value is quite small. The determination of roughness height for different surface types is given by Wieringa [36].

2.3.5. Initial conditions

The fluid mixture composition, height-dependent wind speed, ambient temperature, turbulence kinetic energy, and energy dissipation rate must be specified throughout the domain as initial conditions. These initial values were set close to values in the atmospheric boundary to create an initial state with only wind flow through the domain and no LNG vapor.

3. MKOPSC LNG spill tests

Since 2005 a series of medium-scale LNG spill tests has been carried out with LNG training props at the BFTF by the MKOPSC to study key parameters of vapor dispersion modeling and to collect experimental data for model validation. The props were composed of three concrete pits and one L-shape trench, as shown in Fig. 1. From the several tests performed at BFTF, two sets of test data (06LNG01 and 07LNG01) were selected in the present work since

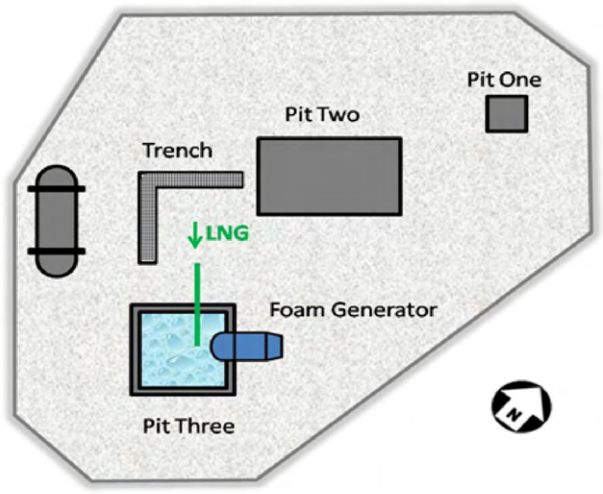

Pit One: 3.05m × 3.05m × 1.22m
Pit Two: 10.06m × 6.4m × 1.22m
Pit Three: 6.71m × 6.71m × 2.44m

Fig. 1. Brayton Fire Training Field LNG props.

they include sufficient information for vapor dispersion simulation setup and evaluation. A brief description of the tests is given as follows.

06LNG01: Pit Three (6.71 m × 6.71 m × 2.44 m) was used to perform this test, which is shown in Fig. 2. The pit was filled with water to the brim. A foam generator (shown on the right-hand side of Fig. 2) was installed at a 1.22 m elevation near the pit to apply high-expansion foam in case of an emergency. A total of approximately 4 m^3 of LNG was released onto the water via a 76-mm-diameter delivery pipe with a flow rate of about 0.265 m^3/min. The large amount of water below the LNG promoted vaporization and kept the vaporization rate essentially equal to the LNG discharge rate. Two weather stations were installed at elevations of 3 and 10 m to collect local weather data, including the wind direction, wind speed, humidity, temperature, and atmospheric pressure. Two thermocouples and two gas detectors were placed in the center of the pit, 1.22 m above the water. Additionally, 16 gas detectors were installed at different downwind distances and elevations (0.30 m and 1.22 m above the ground) to measure the vapor concentration. All of these gas detectors have an accuracy of ±2% (v/v) and their measurement rates are for every second.

07LNG01: Similar to the setup in 06LNG01, Pit Two (10.06 m × 6.4 m × 1.22 m) was filled with water to create a water pond for the LNG release test, as shown in Fig. 3. 1.2-m-high wooden boards were erected around the pit as obstacles. LNG was released onto the water via the same delivery pipe used in 06LNG01 with a flow rate of about 0.75 m^3/min. Two foam generators were installed at a 1.22 m elevation above the pit so as to apply high-expansion foam in the following pool fire test. An array of instrumentation, which was composed of 2 weather conditions, 40 gas detectors, 1 cryogenic flow meter and 92 thermocouples, was utilized at the source area and downwind to measure and record the variables of interest. The setup of poles to support gas detectors is shown in Fig. 4 and the positions of gas detectors are listed in Table 2.

Fig. 2. 06LNG01 test setup.

Fig. 3. 07LNG01 test setup.

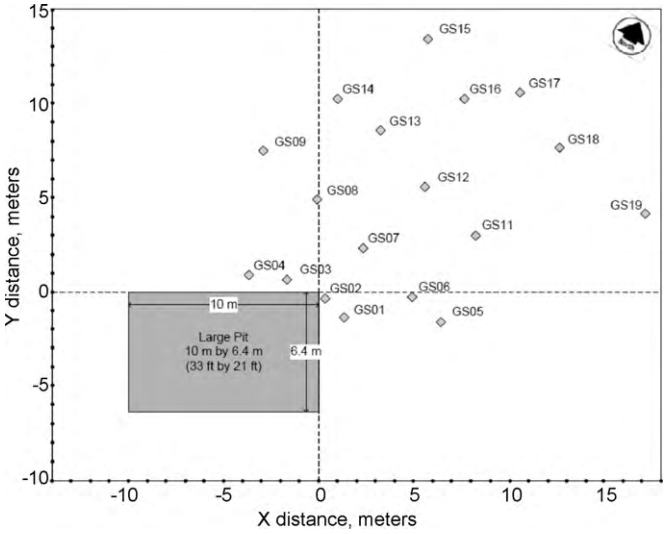

Fig. 4. Gas detector pole setup for 07LNG01 test.

4. Simulation specifications

The simulations were set up using the approach described in the previous section as well as the inputs of necessary data from the tests. For 06LNG01 simulation, the data were exacted from the database over a 45-s time interval, within which there was little variation in wind speed and direction, as shown in Table 3. Therefore, the data can better serve to study the underlying physical mechanism of LNG vapor dispersion and evaluate steady-state simulation results. For 07LNG01 simulation, transient simulations

Table 2
Gas detector positions in 07LNG01 test.

Pole no.	Gas detector position				Pole position in Fig. 4	
	Low	Bottom	Middle	Top	*X* (m)	*Y* (m)
Z, m→	0.50	1.29	2.31	3.30		
GS01	–	GD02	GD01	–	1.2	−1.2
GS02	–	GD05	GD04	GD03	0.4	−0.4
GS03	–	GD08	GD07	GD06	−1.8	0.7
GS04	–	GD10	GD09	–	−3.8	0.8
GS05	–	GD12	GD11	–	6.6	−1.9
GS06	–	GD14	GD 13	–	4.9	−0.2
GS07	–	GD21	GD16	GD15	2.3	2.3
GS08	GD22	GD18	GD17	–	−0.2	4.9
GS09	–	GD 20	GD19	–	−2.8	7.4
GS10	–	–	–	–	–	–
GS11	–	GD32	GD31	–	8.4	2.9
GS12	–	GD26	GD25	–	5.6	5.6
GS13	–	GD28	GD27	–	3.9	7.3
GS14	–	GD30	GD29	–	1.0	10.3
GS15	–	GD24	GD23	–	5.8	13.5
GS16	–	GD34	GD33	–	7.3	10.3
GS17	–	GD35	GD36	–	10.7	10.7
GS18	–	GD38	GD37	–	13.7	7.7
GS19	–	GD40	GD39	–	17.1	4.3

Table 3
Summary of 06LNG01 test data.

Parameter	Value
LNG flow rate (m^3/min)	0.265
LNG pool diameter (m)	4.6[a]
Average wind speed @ 3 m (m/s)	1.8
Average wind speed @ 10 m (m/s)	2.2
Average wind direction @ 3 m (°)	77[b]
Average wind direction @ 10 m (°)	94[b]
Temperature @ 3 m (K)	299.65
Temperature @ 10 m (K)	299.05
Absolute air pressure (Pa)	99860
Relative humidity (%)	64.5
Stability class	D
Monin–Obukhov length (m)	498.3
Roughness height (m)	0.01

[a] Estimated from on-site observation.
[b] 0° is true north.

Table 4
Summary of 07LNG01 test data.

Parameter	Value
LNG flow rate (m^3/min)	0.75
LNG pool diameter (m)	6[a]
Average wind speed @ 2.3 m (m/s)	1.2
Average wind speed @ 10 m (m/s)	1.9
Average wind direction @ 2.3 m (°)	160[b]
Temperature @ 2.3 m (K)	289.05
Temperature @ 10 m (K)	289.05
Absolute air pressure (Pa)	101,300
Relative humidity (%)	32.6
Stability class	B
Monin–Obukhov length (m)	8.3
Roughness height (m)	0.01

[a] Estimated from temperature measurements on the water surface.
[b] 0° is true north.

were conducted to compare downwind gas concentration profiles between test measurements and simulation results over the whole process of LNG release. The input data from 07LNG01 test are shown in Table 4.

Figs. 5 and 6 depict the geometric construction and meshing details of the test scenarios. The entire domain was mainly composed of tetrahedral cells, with a small amount of prism and pyramid cells in the inflation layers to better model the close-to-wall physics of the flow field such as the velocity gradient. Each

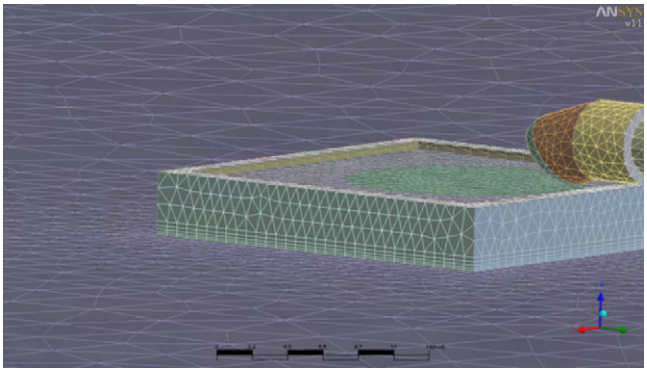

Fig. 5. Geometry construction and meshing details of 06LNG01 test scenario.

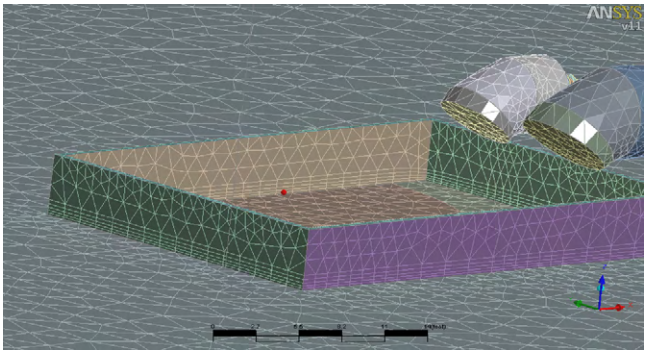

Fig. 6. Geometry construction and meshing details of 07LNG01 test scenario.

simulation was solved using convergence criteria based on a root mean square (RMS) residual of less than 1×10^{-4}. All simulation runs were carried out on a stand-alone desktop using an Intel Core2 Duo CPU E8500 with a clock speed of 3.16 GHz and 3.2 GB of RAM memory.

5. Results and discussion

5.1. Comparison between CFX simulation results and test data

Fig. 7 compares the plume shape of an on-site test photo and the simulation results. The photo was taken approximately 10 min after the start of the test. The visible boundary of the vapor plume corresponded to a vapor concentration of 3.5% (v/v) at a relative humidity of 64.5% [37], which can be represented by an isosurface of identical vapor concentration when post-possessing the simulation results. Fig. 7(a) shows a fog-like vapor cloud that formed as a result of the LNG release on water. The shape of the vapor plume gives an indication of the wind direction at that time. During the test, the vapor cloud wafted down from the edge of the pit and drifted near the ground as a dense gas for a certain distance. As the vapor cloud warmed up, it rose and diluted into the atmosphere. This physical process was reproduced in the CFX simulation, as shown in Fig. 7(b). In both figures, the plume above the pit was almost as high as the foam generator. After the vapor dispersed downward, its volume continued to become larger and larger. The overall height and width of the simulated plume was similar to the real one in source area and downwind. The physical behavior of the LNG vapor dispersion process in the test scenario was well characterized by the ANSYS CFX modeling, especially the vapor buoyancy variation from negative to positive. The effects of the geometry features (foam generator and pit) on the vapor cloud were also well represented.

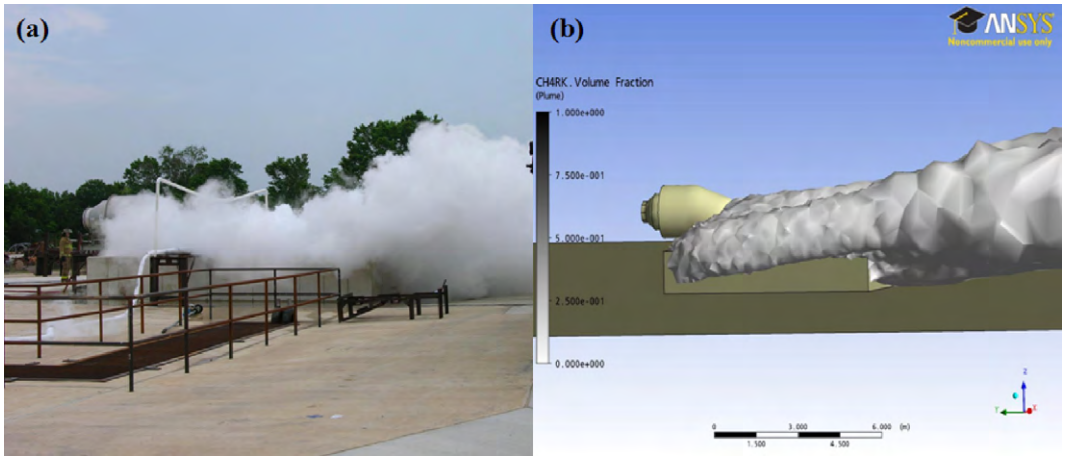

Fig. 7. Comparison of the plume shape of on-site photo and the simulation results. (a) On-site photo and (b) ANSYS CFX simulation.

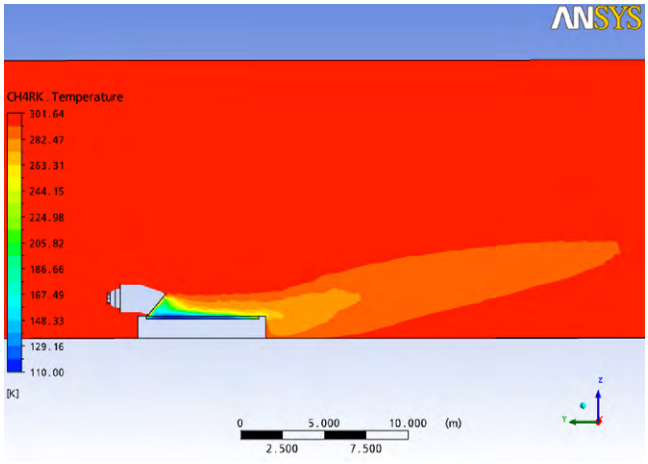

Fig. 8. Vapor temperature in the vertical centerline plane downwind.

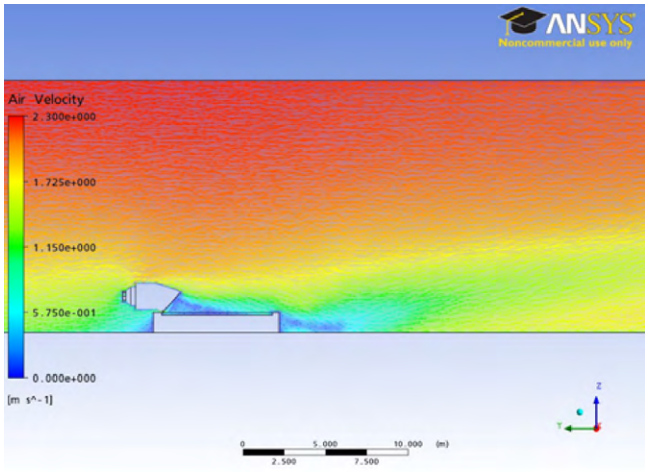

Fig. 9. Air velocity in the vertical centerline plane downwind.

Figs. 8 and 9 show the LNG vapor temperature and air velocity profiles in the downwind vertical centerline plane. The temperature of the LNG vapor changed rapidly after the cold LNG vapor emanated from the pool. At this stage, it mixed with ambient air with intense heat transfer to form a vapor/air mixture. When the mixture drifted downwind, the majority of the heat and momentum transfer occurred at its boundary. As a result, the cloud's core was colder and more stable than its peripheral region. Due to the blockage of the foam generator in the upwind direction, there was a space under the foam generator with little wind and mild mixing with air. Because of this, the temperature of the vapor within this region changed more slowly than that of the vapor away from the foam generator. This indicates that the wind velocity and its turbulence have a strong influence on the temperature change of the vapor cloud and thus on the downwind distance to LFL.

Fig. 10 compares calculated methane volume fraction contours at 0.3 m elevation with contours generated by interpolating scattered experimental data using Kriging method. It is evident that the simulation results are in reasonable overall agreement with test data within the rectangular area where gas detectors were installed to collect vapor concentration data in the test. Due to the effect of wind turbulence on the cloud, it is impossible to make simulated contours accurately match the actual ones. The measured 1/2 LFL distances at elevations of 0.3 and 1.22 m during the test ranged from 8.69 to 13.53 m and from 6.09 to 13.47 m, respectively. Likewise, the simulation results show that the downwind distances to 1/2 LFL at these two elevations were about 9.8 m and 13.4 m, which were within the range of the test data.

Figs. 11–14 compare the predicted gas concentration profiles of 07LNG01 with test measurements at the same locations where gas detectors were installed. Fluctuations in the on-site measurements resulted from the turbulence in the wind. It is noted that simulation results in Fig. 13 provide reasonable overprediction of gas concentrations at 0.5 m elevation above the ground, which is desirable in exclusion zone determination. At 1.29 m elevation, the simulation results in Figs. 11, 12 and 14 fall into the range of concentration fluctuations and show underpredictions of concentration peak values. Moreover, higher gas concentrations appear close to the ground level in the simulation, as illustrated in Figs. 12 and 13, indicating the dense gas behavior of the LNG vapor cloud at the downwind distances where GDs 18 and 22 were located (same location but with different elevations). On the other hand, concentration readings from these two gas detectors reflect that vapors at the bottom have already become positive buoyant and promoted mixing inside the cloud. The over-assumption of dense gas behavior by the simulation therefore results in the underestimation of downwind gas concentrations at higher elevations above the ground, which might be attributed to the incomplete descriptions of heat transfer into the cloud in the simulation setup. The comparison of gas concentrations at two different heights illustrates that CFX is able to give reasonable overpredictions of flammable gas concentrations on the level close to the ground (below 0.5 m) but tends to underestimate

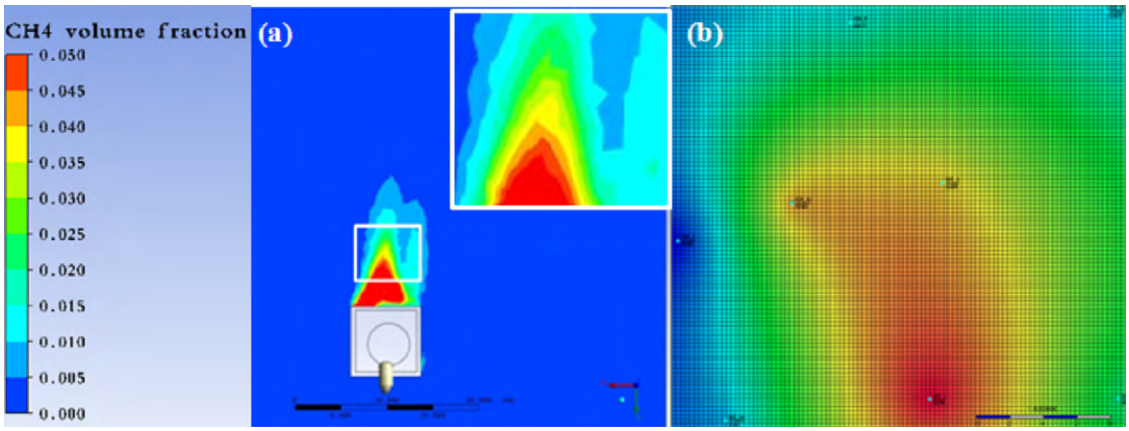

Fig. 10. Methane volume fraction contours at 0.3 m elevation downwind (time = 600 s). (a) ANSYS CFX simulation and (b) test data.

concentrations at higher elevations. It overly assumes the slumping behavior of the LNG vapor cloud in the dispersion process and takes less into account buoyancy change from negative to positive as well as vapor mixing within the cloud.

5.2. Uncertainty sources in the CFX simulation

Uncertainties in CFD simulation results arise from different sources, which can be generally categorized into two groups: (1) numerical errors and uncertainties and (2) errors and uncertainties in modeling the physics [38,39]. The impact of sources in the two categories should be estimated and quantified through a sensitivity analysis in practical applications of CFD codes. If their influence on the accuracy of the simulation results cannot be ignored at certain confidence levels, further study must be carried out on the methods to reduce or control the magnitude. Two examples are given below to illustrate the impact of two parameters, the mesh size and source term turbulence, on the simulation results.

5.2.1. Mesh size effect

Mesh size is a key parameter in controlling spatial discretization, which is associated with the truncation error of Taylor series in the numerical method when calculating flow variable gradients at the face of a control volume. To evaluate the effect of the mesh size on the simulation results, a series of four runs was carried out with the same setup except for the size of the mesh. Table 5 shows the

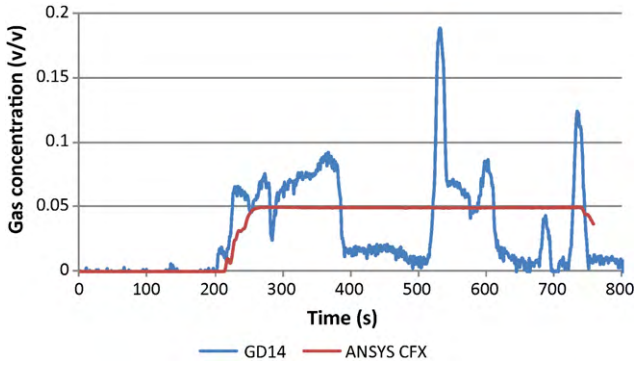

Fig. 11. Comparison of gas concentration in simulation result with test data from GD14 ($x = 4.9$ m, $y = -0.2$ m, $z = 1.29$ m)

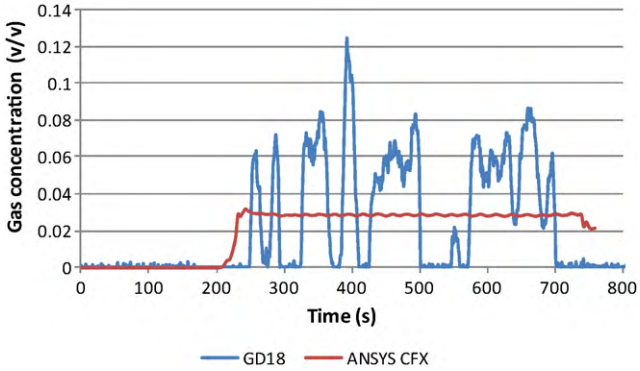

Fig. 12. Comparison of gas concentration in simulation result with test data from GD18 ($x = -0.2$ m, $y = 4.9$ m, $z = 1.29$ m).

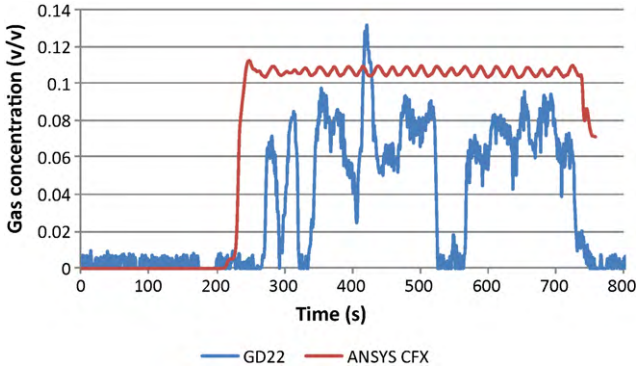

Fig. 13. Comparison of gas concentration in simulation result with test data from GD 22 ($x = -0.2$ m, $y = 4.9$ m, $z = 0.5$ m).

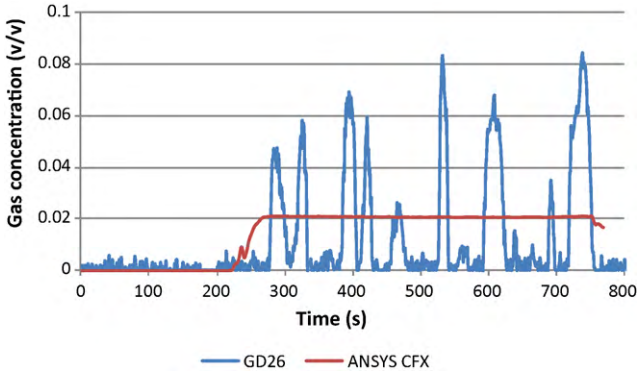

Fig. 14. Comparison of gas concentration in simulation result with test data from GD 26 ($x = 5.6$ m, $y = 5.6$ m, $z = 1.29$ m).

Table 5
Mesh information and simulation results for Runs_1–4.

	Run_1	Run_2	Run_3	Run_4
Maximum spacing (m)	3.66	2.74	1.83	0.91
Total number of nodes	22,391	26,256	51,525	232,687
Total number of tetrahedral	89,536	104,295	199,326	1,074,757
Total number of pyramids	221	222	236	234
Total number of prisms	10,076	11,959	25,870	72,380
Total number of elements	99,833	116,476	225,432	1,147,371
Total running time (min)	11.75	11.9	112.17	92.66
1/2 LFL at 0.3 m elevation (m)	7.7	7.6	10	9.8
1/2 LFL at 1.22 m elevation (m)	17.5	18.3	18.6	13.4

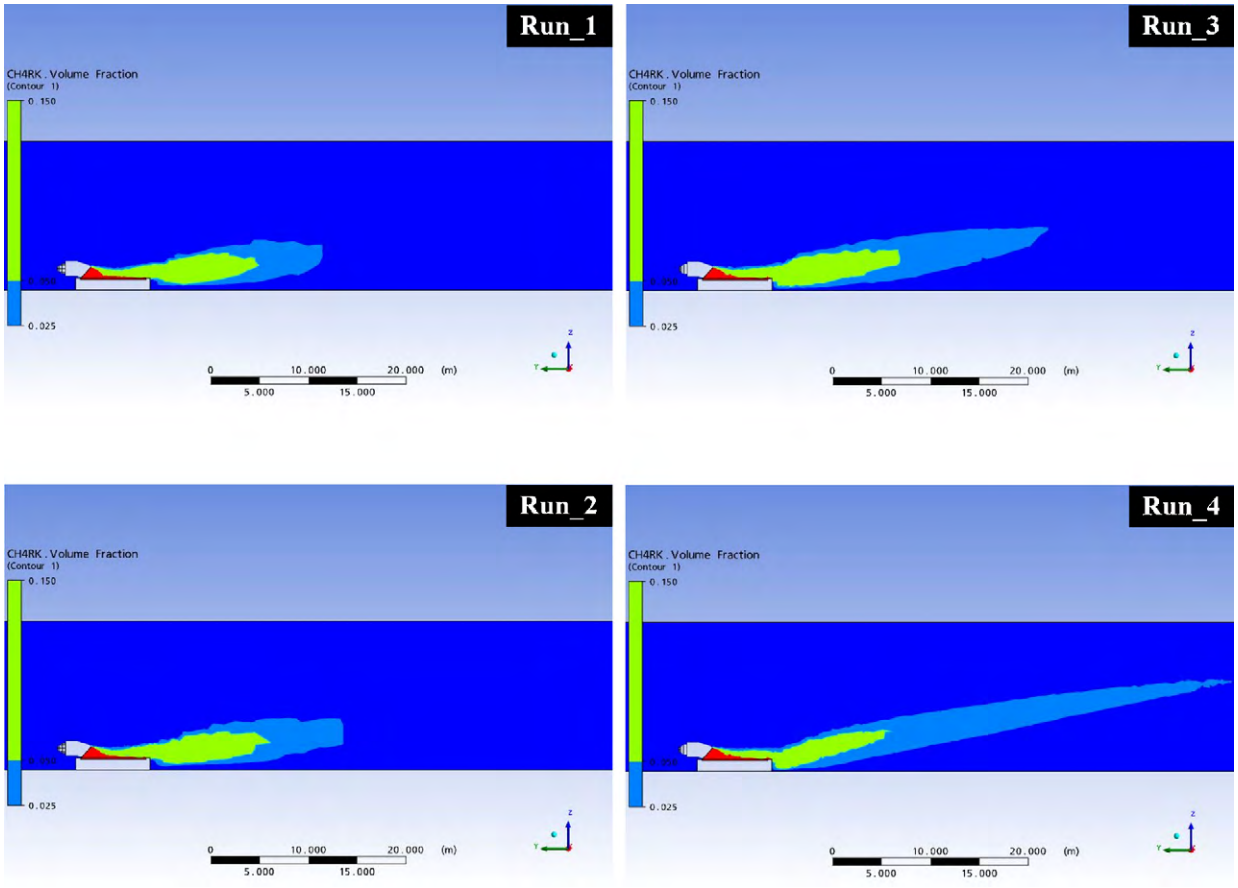

Fig. 15. Vapor fraction contours in the vertical centerline plane for Runs_1–4.

mesh information and simulation results for the 1/2 LFL, in which the maximum spacing was used in ANSYS CFX to set the maximum size of the mesh elements in the background of the domain.

The total running time is determined by the number of iterations and the running time for each iteration, the latter of which is related to the total number of meshing elements. As shown in Table 5, Run_4 had almost five times the number of elements compared to Run_3; therefore it took more time for each iteration. However, Run_3 went through 457 iterations to achieve final convergence while Run_4 only used 82 iterations to obtain the same convergence because of the mesh quality improvement by decreasing mesh size. As a result, the total running time for Run_3 was longer than Run_4.

Table 6
Turbulence intensities and simulation results for Runs_5–8.

	Run_5	Run_6	Run_7	Run_8
Turbulence intensity	1%	5%	10%	20%
1/2 LFL at 0.3 m elevation (m)	0	0	11.2	9.8
1/2 LFL at 1.22 m elevation (m)	4.1	13	11	13.4

Fig. 15 shows contours of the vapor fraction in a downwind vertical centerline plane for Runs_1–4. Here, the 0.15 (UFL), 0.05 (LFL), and 0.025 (1/2 LFL) vapor volume fraction levels were of interest and were monitored to study the mesh size effect.

Due to insufficient number of meshing elements, the simulated vapor cloud did not depict a similar pattern as the cloud recorded in the experiment. A reliable numerical prediction could not be achieved with the default mesh size (Run_1). A finer mesh is required to reach desirable simulation accuracy. As shown in Fig. 15, when the mesh size was gradually decreased to 0.91 m (Run_4), the calculated 1/2 LFL at elevations of 0.3 and 1.22 m fell into the test data range.

In this study, a mesh-independent solution could not be achieved by repeating the calculations with successively refined meshes due to the limited available memory and computing power. For similar industrial cases, it is recommended to run simulations with two or three gradually decreasing mesh sizes and to compare the results to estimate the solution accuracy.

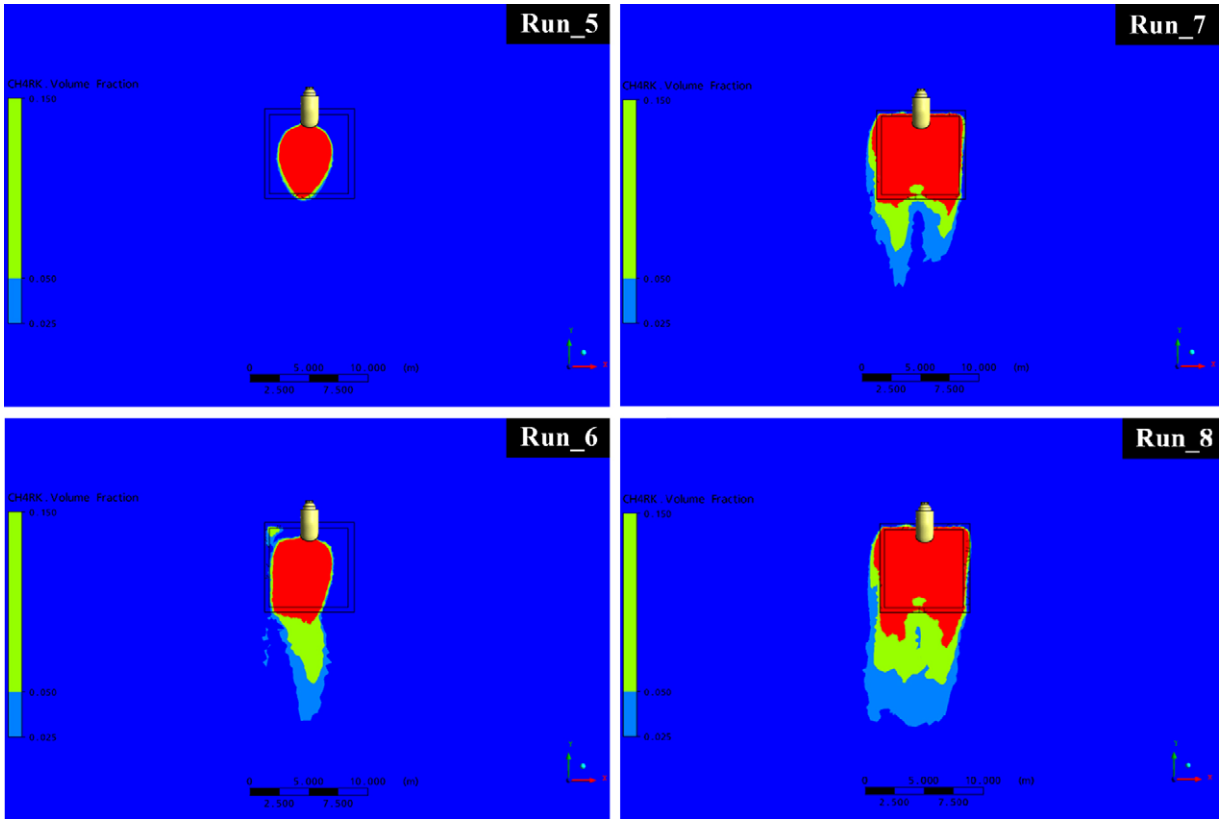

Fig. 16. Vapor fraction contours at an elevation of 1.22 m for Runs_5–8.

5.2.2. Source term turbulence intensity effect

Another important parameter is the turbulent intensity in the source term which is associated with modeling vapor dispersion physical process. Turbulence intensity is the ratio of the standard deviation of the turbulent velocity fluctuations to the mean velocity. It characterizes the turbulence violence and determines the kinetic energy and energy dissipation rate above the pool based on Eqs. (26) and (27). A series of four simulations were performed with different values of turbulence intensity in the source term to explore its influence on the simulation results. Table 6 shows the turbulence intensities and simulation results for the 1/2 LFL.

Fig. 16 shows vapor fraction contours at an elevation of 1.22 m for Runs_5–8. In Run_5, where the level of turbulence is quite low, all volume fraction contours (UFL, LFL, and 1/2 LFL) almost overlapped. As the turbulent intensity gradually increased to 20% (Run_8), the predicted distance of the 1/2 LFL changed to almost three times the length of that given by Run_5. Thus, changing the turbulence intensity influences the shape of the vapor cloud and the prediction accuracy of the distance to flammable ranges.

6. Conclusions

We used a CFD code to investigate LNG vapor dispersion modeling, and validated the simulation results against medium-scale LNG spill tests at the BFTF. We identified essential parameters to setup a CFD simulation and discussed the uncertainties in simulation results. Generally, CFD is able to effectively describe the dense gas behavior of LNG vapor dispersion in the atmosphere, and with appropriate setup inputs its prediction results provide good approximation of safe separation distances on the level near the ground. Our simulated results also showed that CFX gave concentration underpredictions at higher elevations (e.g., at 1.29 m elevation) because of the over-assumption of dense gas behavior of LNG cloud in the simulation. The authors believe that complete representations of heat transfer from various sources to the LNG vapor cloud could contribute to the improvement of reliability of CFX prediction results. Moreover, some numerical or physical parameters, such as mesh size and source term turbulent intensity, have a significant impact on the simulation accuracy. We recommend using a sensitivity analysis to estimate and reduce the magnitude of errors related to numerical solution methods. To obtain the best possible prediction results out of CFX with available computing resources, more experimental work is needed to study the parameters that are essential to characterize the physical process of LNG vapor dispersion.

Acknowledgements

The authors would like to thank BP Global Gas SPU for their financial support and guidance during the test. Special acknowledgment also goes to ABB Inc. and the Brayton Fire Training Field for providing test support.

References

[1] M. Hightower, L. Gritzo, A. Luketa-Hanlin, J. Covan, S. Tieszen, G. Wellman, M. Irwin, M. Kaneshige, B. Melof, C. Morrow, D. Ragland, Guidance on Risk Analysis and Safety Implications of a Large Liquefied Natural Gas (LNG) Spill Over Water, SAND2004-6258, Sandia National Laboratories, Albuquerque, NM, 2004.
[2] V.L. Thorndike, LNG: A Level-Headed Look at the Liquefied Natural Gas Controversy, Down East Books, 2007.
[3] J.A. Alderman, Introduction to LNG safety, Process Saf. Prog. 24 (2005) 144–151.
[4] Title 49 Code of Federal Regulations Part 193(49-CFR-193): Liquefied Natural Gas Facilities: Federal Safety Standards, U.S. Government Printing Office, Washington, DC, 1980.
[5] National Fire Protection Association (NFPA), NFPA 59A: Standard for the Production, Storage, and Handling of Liquefied Natural Gas (LNG), NFPA, Quincy, MA, 2009.
[6] T.O. Spicer, J.A. Havens, Field test validation of the DEGADIS model, J. Hazard. Mater. 16 (1987) 231–245.

[7] D.L. Ermak, S.T. Chan, D.L. Morgan, L.K. Morris, A comparison of dense gas dispersion model simulations with burro series LNG spill test results, J. Hazard. Mater. 6 (1982) 129–160.
[8] J.S. Puttock, Comparison of Thorney Island data with predictions of HEGABOX/HEGADAS, J. Hazard. Mater. 16 (1987) 439–455.
[9] A. Luketa-Hanlin, A review of large-scale LNG spills: experiments and modeling, J. Hazard. Mater. 132 (2006) 119–140.
[10] A. Luketa-Hanlin, R.P. Koopman, D.L. Ermak, On the application of computational fluid dynamics codes for liquefied natural gas dispersion, J. Hazard. Mater. 140 (2007) 504–517.
[11] S.T. Chan, Numerical simulations of LNG vapor dispersion from a fenced storage area, J. Hazard. Mater. 30 (1992) 195–224.
[12] F. Gavelli, E. Bullister, H. Kytomaa, Application of CFD (fluent) to LNG spills into geometrically complex environments, J. Hazard. Mater. 159 (2008) 158–168.
[13] S. Sklavounos, F. Rigas, Simulation of Coyote series trials—Part I: CFD estimation of non-isothermal LNG releases and comparison with box-model predictions, Chem. Eng. Sci. 61 (2006) 1434–1443.
[14] O.R. Hansen, J.A. Melheim, I.E. Storvik, CFD modeling of LNG dispersion experiments, in: AIChE Spring National Meeting, Houston, TX, 2007.
[15] B.R. Cormier, R. Qi, G. Yun, Y. Zhang, M.S. Mannan, Application of computational fluid dynamics for LNG vapor dispersion modeling: a study of key parameters, J. Loss Prevent. Proc. Ind. 22 (2009) 332–352.
[16] ANSYS CFX-Solver Theory Guide, ANSYS Ltd., 2006.
[17] N. Ashgriz, J. Mostaghimi, An introduction to computational fluid dynamics, in: J. Saleh (Ed.), Fluid Flow Handbook, McGraw-Hill Professional, 2002, pp. 24.1–24.52.
[18] M.J. Ivings, S.F. Jagger, C.J. Lea, D.M. Webber, Evaluating Vapor Dispersion Models for Safety Analysis of LNG Facilities, Health & Safety Laboratory, UK, 2007.
[19] ANSYS CFX-Post User's Guide, ANSYS Ltd., 2006.
[20] H.K. Versteeg, W. Malalasekera, An Introduction to Computational Fluid Dynamics: The Finite Volume Method, second ed., Prentice Hall, 2007.
[21] H.A. Olvera, A.R. Choudhuri, Numerical simulation of hydrogen dispersion in the vicinity of a cubical building in stable stratified atmospheres, Int. J. Hydrogen Energy 31 (2006) 2356–2369.
[22] Release 11.0 Documentation for ANSYS Workbench, ANSYS Ltd., 2006.
[23] M.M. Foss, Introduction to LNG: An Overview on Liquefied Natural Gas (LNG), It Properties, Organization of the LNG Industry and Safety Considerations, Center for Energy Economics, University of Texas at Austin, Houston, TX, 2007.
[24] Institution of Chemical Engineers (IChemE), BP Process Safety Series-LNG Fire Protection & Emergency Response, IChemE, UK, 2007.
[25] S. Sklavounos, F. Rigas, Validation of turbulence models in heavy gas dispersion over obstacles, J. Hazard. Mater. 108 (2004) 9–20.
[26] G.A. Perdikaris, F. Mayinger, Numerical simulation of heavy gas cloud dispersion within topographically complex terrain, J. Loss Prevent. Proc. Ind. 7 (1994) 391–396.
[27] B. Blocken, T. Stathopoulos, J. Carmeliet, CFD simulation of the atmospheric boundary layer: wall function problems, Atmos. Environ. 41 (2007) 238–252.
[28] T.C. Brown, R.T. Cederwall, S.T. Chan, D.L. Ermak, R.P. Koopman, K.C. Lamson, J.W. McClure, L.K. Morris, Falcon Series Data Report: 1987 LNG Vapor Barrier Verification Field Trials, Lawrence Livermore National Laboratory, June 1990, UCRL-CR-104316.
[29] S.P. Arya, Introduction to Micrometeorology, second ed., Academic Press, 2001.
[30] H.A. Panofsky, J.A. Dutton, Atmospheric Turbulence: Models and Methods for Engineering Applications, Wiley, New York, 1984.
[31] P.J. Richards, R.P. Hoxey, Appropriate boundary conditions for computational wind engineering models using the k–ε turbulence model, J. Wind Eng. Ind. Aerodynam. 46–47 (1993) 145–153.
[32] D.W. Hissong, Keys to modeling LNG spills on water, J. Hazard. Mater. 140 (2007) 465–477.
[33] F. Briscoe, P. Shaw, Spread and evaporation of liquid, Prog. Energy Comb. Sci. 6 (1980) 127–140.
[34] J.A. Fay, Model of spills and fires from LNG and oil tankers, J. Hazard. Mater. 96 (2003) 171–188.
[35] B.R. Cormier, J. Suardin, M. Rana, Y. Zhang, Development of design and safety specifications for LNG facilities based on experimental and theoretical research, in: E.R. Pitt, C.N. Leung (Eds.), OPEC, Oil Prices and LNG, Nova Science Publishers, 2009.
[36] J. Wieringa, Updating the Davenport roughness classification, J. Wind Eng. Ind. Aerodynam. 41 (1992) 357–368.
[37] P.K. Raj, Where in a LNG vapor cloud is the flammable concentration relative to the visible cloud boundary, NFPA J. May/June (2006).
[38] H.W. Coleman, F. Stern, Uncertainties and CFD code validation, J. Fluids Eng. 119 (1997) 795–803.
[39] J. Tu, G.H. Yeoh, C. Liu, Computational Fluid Dynamics—A Practical Approach, Butterworth–Heinemann, Oxford, UK, 2008.